IEEE Access
Multidisciplinary | Rapid Review | Open Access Journal

Received August 29, 2018, accepted October 28, 2018, date of publication November 14, 2018,
date of current version December 18, 2018.

Digital Object Identifier 10.1109/ACCESS.2018.2881261

Statics of Continuum Space Manipulators With Nonconstant Curvature via Pseudorigid-Body 3R Model

SHAOPING HUANG[1], DESHAN MENG[1,2], YU SHE[3], XUEQIAN WANG[1,2], BIN LIANG[2], (Member, IEEE), AND BO YUAN[1,2], (Member, IEEE)

[1]Center for Artificial Intelligence and Robotics, Graduate School at Shenzhen, Tsinghua University, Shenzhen 518055, China
[2]Department of Automation, Tsinghua University, Beijing 100084, China
[3]Computer Science and Artificial Intelligence Laboratory, Massachusetts Institute of Technology, Cambridge, MA 02139, USA

Corresponding authors: Xueqian Wang (wang.xq@sz.tsinghua.edu.cn) and Bin Liang (liangbin@tsinghua.edu.cn)

This work was supported in part by the China Postdoctoral Science Foundation under Grant 2018M631473, in part by the National Natural Science Foundation of China under Grant 61673239, in part by the Guangdong Natural Science Foundation under Grant 2018A030310679, and in part by the Basic Research Program of Shenzhen under Grant JCYJ20170412171459177 and Grant JCYJ20160301100921349).

ABSTRACT Continuum space manipulators have wide application prospect in the complex space environment with small space. Efficient and accurate static models are very important for continuum manipulators. However, the existing static models of cable-driven continuum manipulators, which are based on theories of elasticity, are often very complex and not conducive to efficient computing. In this work, the cable-driven continuum manipulator is equivalent to the traditional rigid one by the pseudorigid-body 3R model. We establish the static equation of the continuum manipulator, which takes into account the effects of friction, multi-segment coupling, and external loads. The calculation speed of the static equation obtained by the proposed method is 16.52 times that of obtained by the traditional integration method. Then, the effects of the magnitude and direction of the friction on the curvature and configuration of the manipulator are discussed, respectively. The influences of the configuration and stiffness of the manipulator on the coupling between the segments are also studied. Through the coupling analysis of different stiffness, we give some advice to the design of multi-segment continuum manipulators. Finally, the experiments are made through a two-segment continuum manipulator to validate the proposed static model. The maximum position error between the simulation and experimental results is 5.57%.

INDEX TERMS Continuum manipulator, pseudorigid-body 3R model, friction, static coupling, on-orbit service.

I. INTRODUCTION

Space manipulators play an increasingly important role in future space activities such as repairing, upgrading, and refueling spacecraft. However, conventional space manipulator systems, such as the Space Station Remote Manipulator System (SSRMS), European Robotic Arm (ERA), Japanese Experiment Module Remote Manipulator System (JEMRMS), Shuttle Remote Manipulator System (SRMS) [1]–[3], cannot be applied in the non-structural narrow environment due to the limitation of its own structural characteristics. The backbone of continuum manipulator, which has high redundancy and even theoretically infinite degrees of freedom [4], [5], is elastic material. This structure feature gives the continuum manipulator excellent motion flexibility, which is suitable for obstacle avoidance in narrow space. The compliance, flexibility and thinness of continuum manipulator make it have wide application prospect in the complex environment with small space. For example, the continuum space manipulator has the ability to penetrate deeply into the spacecraft for detection and maintenance by crossing the truss structure and component clearance.

The constant curvature kinematics is widely used in the continuum manipulator [6], but the actual model is often not constant curvature [7]. In order to establish an accurate model, the effects of external forces, friction and elastic force should be considered [8], [9]. The general theories of elasticity and energy minimization method are widely used to deal with the static problems of continuum

manipulators [10]. The Cosserat rod theory is used to represent the manipulator as a curve in space with relevant elasticity, actuation, and gravitational forces considered for a cable-driven robot [11]. Rucker *et al.* [12] had used the Kirchhoff rod theory to build the static model of concentric tube continuum manipulators. The method based on the Bernoulli-Euler beam model [10] is mainly used on the concentric tube continuum manipulators, and the simple plane bending effect. But the equations of Bernoulli-Euler beam model contain integral term, which results in inefficient calculations and the inability to extract parameters for specific analysis [13]. The principle of virtual power based on constant curvature is used in cable-driven continuum manipulators to discuss the control methods of friction and driving force [14]. Moreover, many researchers have carried out more detailed studies on various aspects of cable-driven continuum manipulators. Rucker *et al.* [9], [15] used the principle of virtual power to analyze the external loading, but did not consider the influence of friction which lead to the primary error of his model. Yuan and Li [16] proposed a method of analyzing the workspace of a cable-driven continuum manipulator by using static analysis which takes into account the internal cable tension, the external payload and the gravity force. Yuan *et al.* [17] also proposed a new force sensing method based on the shape reconstruction algorithm and the robot kinematic-static model. Rone and Ben-Tzvi [18] discussed the frictional effects of a multi-segment cable-driven continuum manipulator, and the coupling effects between two segments. However, the external loading is not considered and the coupling effects are not qualitatively discussed in [18].

Since the same static state of the manipulator may have different static friction coefficients and static friction forces, which are caused by the difference in the motion state of the manipulator, it is difficult to qualitatively discuss the influence of static friction force in the equilibrium state on the cable-driven continuum manipulator. Some researchers have conducted preliminary research on the influence of friction on the statics of cable-driven continuum manipulators [19], [20]. In this paper, we are committed to the study of high computational efficiency and high precision static modeling methods for continuum manipulators. Based on the pseudo-rigid body (PRB) 3R theory proposed by Su [21], the static model of a multi-segment cable-driven continuum manipulator is established. By using this model, the influence of friction is analyzed and mechanical coupling effects have been discussed deeply, which can provide some references for the design of multi-segment cable-driven continuum manipulators.

This paper is organized as follows: In the section II, a continuum manipulator consisting of spring plates is introduced and its static model is derived. Then we discuss the efficiency of the model. Section III discusses the frictional and the coupling effects on the continuum manipulator. Section IV details the cross-validation of the PRB 3R method simulations compared with numerical models and experimental results. Section V summarizes the results and describes the future work.

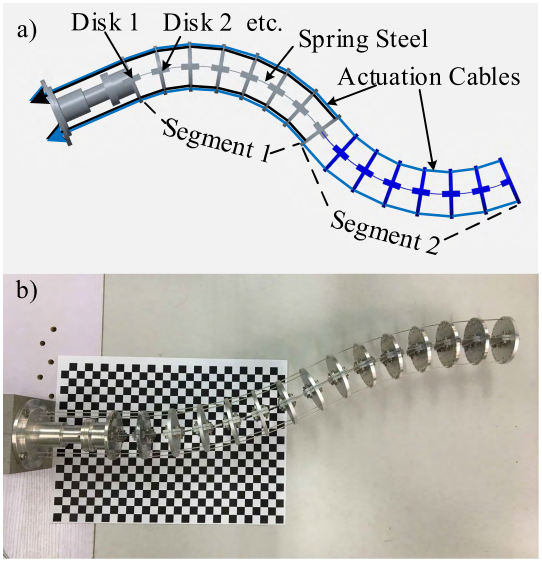

FIGURE 1. a) The structure of the cable driven multi-segment continuum manipulator; b) The prototype of the continuum manipulator.

II. STATICS MODELING

In this section, the static modeling of a continuum manipulator with two segments is provided. The structure of the continuum manipulator is illustrated in Fig.1. As shown, the continuum manipulator consists of two segments, either of which is divided into seven sub-segments by a series of disks. Each two disks are connected by a spring steel plate which is the key component used to realize the deformation movement of the manipulator. There are cable holes on both sides of these disks, and spring steel plates achieve the desired bending by changing the lengths and/or tensions of the driving cables. There are four cables on the same horizontal plane and each section is driven by two cables. The advantage of this structure is that it has high strength and good deformation ability, and that it will have better effect on the large size continuum mechanism. The deformation of the spring steel can be analyzed by using the large deflection beam theory.

A. STATICS MODELING OF SUBSEGMENTS

As described in the above section, the key to model this manipulator is to analyze the bending deformation of the spring steel. The traditional beam theory and the elliptic integral method are used to analyze the bending of the intermediate spring steel, respectively [22], [23]. But it will be very complicated to solve equations because of the integral term. In this section, we propose a new method based on the PRB 3R model to analyze the manipulator. Here R represents a revolute or pin joint.

A PRB 1R model is enough to analyze a simple deformation where a constant force or torque is applied at the end of the beam. However, the PRB 1R model is not suitable for the

continuum manipulator because the equivalent force applied to the tip of the beam is variable. We adopt a PRB 3R model proposed by Su [21] to solve the static model of subsegments. The PRB 3R model can control the error within 1% even the beam has a large deformation [21]. The essence of this method is that a beam with a length of l is equivalent to four rigid links joined by three torsion springs. The key is to solve the static constraint equations of these three torsion springs as shown in (1):

$$\begin{pmatrix} \tau_1 \\ \tau_2 \\ \tau_3 \end{pmatrix} = [\boldsymbol{J}^{\mathrm{T}}] \begin{pmatrix} F_x l \\ F_y l \\ M_0 \end{pmatrix}, \tag{1}$$

where τ_1, τ_2 and τ_3 are the torsion forces corresponding to the three torsion springs, $\boldsymbol{J}^{\mathrm{T}}$ is the matrix which consists of the deflection angle of three torsion springs and the characteristic radius factor γ, F_{x}, F_{y} and M_0 are the tip loads, and l is the length of the beam.

In this model, all the external forces containing cable tensions and external loads will be used to calculate the moment on the right side of (2). The friction force and pressure between cable and cable hold will be used to calculate the cable tensions. The static equation for each torsion spring is established as follows:

$$\tau_{i,k} = \boldsymbol{M}_{i,k}^{\mathrm{cable}} + \boldsymbol{M}_{i,k}^{\mathrm{ext}}, \tag{2}$$

where $i \in$ [1 subseg] is the number of subsegment. Here subseg represents the total number of subsegments and subseg $= 14$. $k \in$ [1 3] is the number of the torsion spring in the Subsegment i. $\boldsymbol{M}_{i,k}^{\mathrm{cable}}$ is the equivalent moment of the cable forces applied to the torsion spring, and $\boldsymbol{M}_{i,k}^{\mathrm{ext}}$ is the equivalent moment of the external loads applied to the torsion spring. When the cable tensions and external force are given, all the equivalent pseudorigid body angles can be obtained by (2). Therefore, both the configuration and the end pose of the manipulator can be calculated.

Fig.2(a) shows a subsegment of the continuum manipulator. The geometry of each subsegment is the same. The spring steel plant is sandwiched between two disks. The length of the clamping structure is a. Parameters L and t are the length of the spring steel plant and the thickness of the disk, respectively. The length of the middle curved arc is $l = L\text{-}2a$. $\boldsymbol{F}$ represents the cable tension through this subsegment. Under the action of this force, the spring steel plant will bend, which can be equivalent to the PRB 3R model shown in Fig.2(b). For the convenience of describing the continuum manipulator, we set the connection point between the spring steel plant belonging to the Subsegment i and the Disk i as the coordinate system origin of this subsegment. The x-axis points in the direction of the spring steel plant's length, and the y-axis points in the direction perpendicular to the spring steel plant's plane, as shown in Fig.2(b). We define $\boldsymbol{O}_1$ as the origin of the world coordinate system. $K_{i\in[13]}$ and $\gamma_{i\in[03]}$ are the stiffness coefficient of three torsion springs and the characteristic radius factor, respectively. $h_{j\in[14]}$ is the distance from the jth cable hole to the center of the disk.

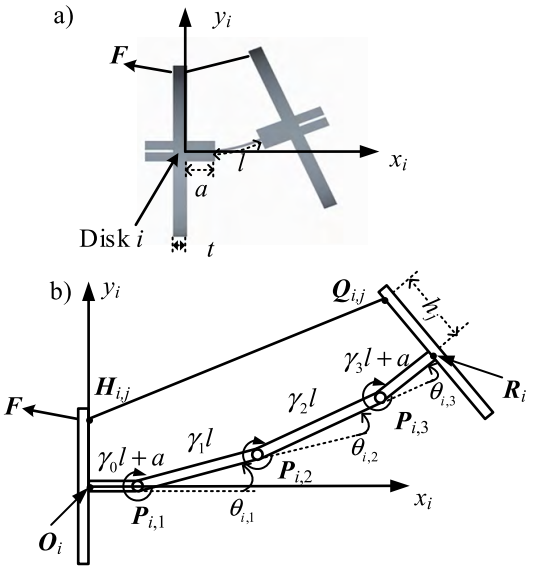

FIGURE 2. a) Sketches of the force in a subsegment; b) The PRB 3R model for a subsegment subject to a cable force.

$\boldsymbol{Q}_{i,j\in[14]}$ and $\boldsymbol{H}_{i,j\in[14]}$ are the distal and proximal cable holes of the Subsegment i. $\boldsymbol{P}_{i,j\in[13]}$ are the positions of three torsion springs. $\boldsymbol{R}_i$ is the connection point between the spring steel plant belonging to the Subsegment i and the Disk $i+1$. $\boldsymbol{O}_i$ is the origin of the Subsegment i. $\theta_{i,j\in[13]}$ is the deflection angle of the jth torsion spring. $\theta_{i,0}$ represents the tip slope angle of the Subsegment i and $\theta_{i,0} = \theta_{i,1} + \theta_{i,2} + \theta_{i,3}$.

We can get the homogeneous transformation matrix $\boldsymbol{T}_i$ (from $\boldsymbol{O}_i$ transform to $\boldsymbol{O}_{i+1}$) in this subsegment, as shown in (3):

$$\boldsymbol{T}_i = \boldsymbol{T}_{i,0}\boldsymbol{T}_{i,1}\boldsymbol{T}_{i,2}\boldsymbol{T}_{i,3}\boldsymbol{T}_{i,4}, \tag{3}$$

where $\boldsymbol{T}_{i,0}$ is the transformation matrix from $\boldsymbol{O}_i$ to $\boldsymbol{P}_{i,1}$, $\boldsymbol{T}_{i,1}$ is the transformation matrix from $\boldsymbol{P}_{i,1}$ to $\boldsymbol{P}_{i,2}$, $\boldsymbol{T}_{i,2}$ is the transformation matrix from $\boldsymbol{P}_{i,2}$ to $\boldsymbol{P}_{i,3}$, $\boldsymbol{T}_{i,3}$ is the transformation matrix from $\boldsymbol{P}_{i,3}$ to $\boldsymbol{R}_i$ and $\boldsymbol{T}_{i,4}$ is the transformation matrix from $\boldsymbol{R}_i$ to $\boldsymbol{O}_{i+1}$, respectively. $\boldsymbol{T}_{i,j}$ is calculated by the following function:

$$\mathrm{T}_{i,j} = \begin{bmatrix} \cos\theta_{i,j} & -\sin\theta_{i,j} & 0 & \Gamma_j \cos\theta_{i,j} \\ \sin\theta_{i,j} & \cos\theta_{i,j} & 0 & \Gamma_j \sin\theta_{i,j} \\ 0 & 0 & 1 & 0 \\ 0 & 0 & 0 & 1 \end{bmatrix}, \quad j = 0, 1, 2, 3, 4, \tag{4}$$

where $\theta_{i,0} = \theta_{i,4} = 0$, $\Gamma_0 = \gamma_0 l + a$, $\Gamma_1 = \gamma_1 l$, $\Gamma_2 = \gamma_2 l$, $\Gamma_3 = \gamma_3 l + a$ and $\Gamma_4 = t$.

Through the transformation matrix, we can use the deflection angles of the torsion springs to calculate the positions of each operating points, such as $\boldsymbol{Q}_{i,j}$, $\boldsymbol{P}_{i,j}$, $\boldsymbol{H}_{i,j}$, and $\boldsymbol{R}_i$, and the entire configuration of the manipulator.

B. STATIC EQUILIBRIUM EQUATIONS

In section II-A, the static equations of the deformation unit are established. In this section, the static model of the

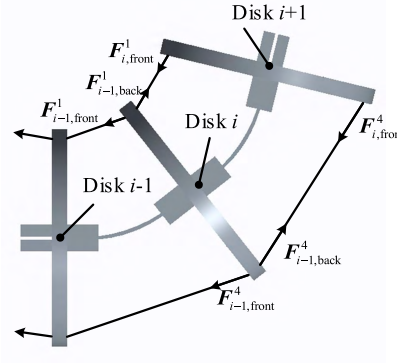

FIGURE 3. The force analysis between two subsegments.

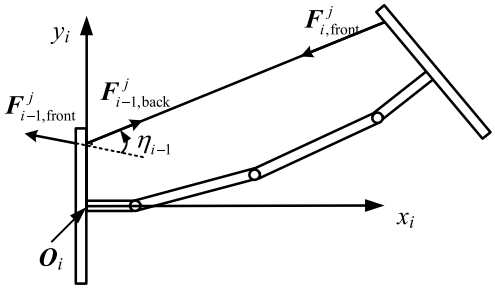

FIGURE 4. The geometric relationship between the force of the cable *j* transfer from Disk *i* −1 to Disk *i*.

whole manipulator would be derived, taking into account the effects of inter-segment coupling, frictional and external loads.

Fig.3 shows the deformation of the manipulator when the 1st and the 4th cables are being pulled. The force analysis of the *i*th spring steel plant corresponding to the Disk *i* is carried out by partition method. This method is only affected by cable tension $\boldsymbol{F}^j_{i,\text{front}}$ applied to the *j*th cable in Disk *i* and external force $\boldsymbol{F}^{\text{ext}}$ applied to the manipulator. The 'front' means the direction from the tip to the bottom in a segment and the 'back' is the reverse direction.

1) $\boldsymbol{p}^j_{i,\text{front}}$ is the direction of cable tension $\boldsymbol{p}^j_{i,\text{front}}$, which can be represented as the unit vector from $\boldsymbol{Q}_{i,j}$ to $\boldsymbol{P}_{i,j}$ as follows:

$$\boldsymbol{p}^j_{i,\text{front}} = (\boldsymbol{P}_{i,j} - \boldsymbol{Q}_{i,j}) / \left\| \boldsymbol{P}_{i,j} - \boldsymbol{Q}_{i,j} \right\|. \tag{5}$$

The magnitude of $\boldsymbol{p}^j_{i,\text{front}}$ can be calculated by belt friction equation [24]. Fig.4 shows the geometric relationship of the force of the *j*th cable in Disk *i*. A belt friction model is used to deal with the friction between the cable hole and the cable due to the "wrap" of the cabling around the cable routing holes, as illustrated in Fig.5 (a). Fig.5 (b) shows the key parameters of the belt friction model.

According to the friction model of the cable routing holes shown in [14, Fig. 5], we have the following function:

$$\left\| \boldsymbol{F}^j_{i,\text{front}} \right\| = \left\| \boldsymbol{F}^j_{i-1,\text{back}} \right\| = \left\| \boldsymbol{F}^j_{i-1,\text{front}} \right\| e^{s\mu\eta_{i-1}}. \tag{6}$$

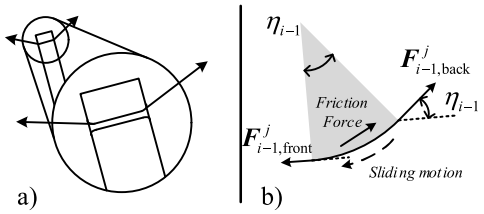

FIGURE 5. a) Cut-away view of cable-disk contact; b) Assumed belt friction model for cable-disk contact.

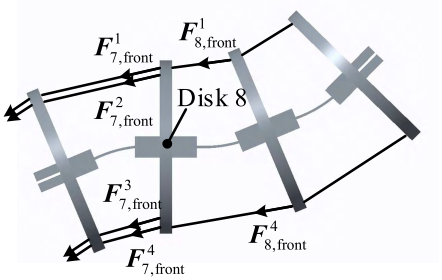

FIGURE 6. Transfer of the cable force from Segment 1 to Segment 2.

$\boldsymbol{F}^j_{0,\text{front}}$ is the driving force which is the input of the equations. The parameter s depends on the direction of the sliding motion of the cable. The value of s is 1 or −1. We define the value of s corresponding to the direction of sliding motion of the cable shown in Fig.5(b) as −1. μ is the coefficient of kinetic friction. The contact angle η_{i-1} can be obtained by the angle between $-\boldsymbol{P}^j_{i,\text{front}}$ and $\boldsymbol{P}^j_{i-1,\text{front}}$:

$$\eta_{i-1} = \pi - < -\boldsymbol{p}^j_{i,\text{front}}, \boldsymbol{p}^j_{i-1,\text{front}} > . \tag{7}$$

Given the driving force of the rope, the tension of the cable at each disc can be iterated by (6). Therefore, the resulting actuation moment $\boldsymbol{M}^{\text{cable}}_{i,k}$ on the torsion springs can be computed as follows:

$$\boldsymbol{M}^{\text{cable}}_{i,k} = \sum_{j=1}^{4} \boldsymbol{F}^j_{i,\text{front}} \times (\boldsymbol{P}_{i,k} - \boldsymbol{Q}_{i,j}), \quad k = 1, 2, 3. \tag{8}$$

In addition, considering the change in the number of cables transferred from the first segment to the second segment of the manipulator, there are four cables in the first segment and only Cables 1 and 4 in the second segment have effects on the manipulator. The special transformation, which is between Segment 1 and Segment 2, from Disk 8 to Disk 9 is illustrated in Fig.6. So starting with Disk 8, Cables 2 and 3 have no effects on the manipulator. The expression of the action moment of the cable force on the torsion spring k of Steel i shown in (9).

$$\boldsymbol{M}^{\text{cable}}_{i,k} = \begin{cases} \sum_{j=1}^{4} \boldsymbol{F}^j_{i,\text{front}} \times (\boldsymbol{P}_{i,k} - \boldsymbol{Q}_{i,j}) \; i \le 7 \\ \boldsymbol{F}^1_{i,\text{front}} \times (\boldsymbol{P}_{i,k} - \boldsymbol{Q}_{i,4}) + F^4_{i,\text{front}} \times (\boldsymbol{P}_{i,k} - \boldsymbol{Q}_{i,4}) \; i > 7. \end{cases} \tag{9}$$

TABLE 1. The parameters of prb 3r model.

K_1	K_2	K_3	γ_0	γ_1	γ_2	γ_3
$3.25\frac{EI}{l}$	$2.84\frac{EI}{l}$	$2.95\frac{EI}{l}$	0.125	0.35	0.388	0.136

TABLE 2. The comparation of the prb 3r model and the integral model in computation speed.

Number of Iterations	Operation time of integral model	Operation time of PRB 3R model	Speed of PRB/Speed of Integral	Maximum position error
20	37.51s	2.27s	16.52	0.081%

2) We define the point of external forces applied to the manipulator is $\boldsymbol{S}$. Therefore the moment applied to the torsion spring k will be calculated as shown in (10):

$$\boldsymbol{M}_{i,k}^{\text{ext}} = \boldsymbol{F}^{\text{ext}} \times (\boldsymbol{P}_{i,k} - \boldsymbol{S}), \quad k = 1, 2, 3. \tag{10}$$

The spring torque $\tau_{i,k}$ in (2) can be expressed according to the assumption below. The spring torques are proportional to the PRB angles of PRB 3R model, i.e.,

$$\tau_{i,k} = K_k \theta_{i,k}, \quad k = 1, 2, 3. \tag{11}$$

Substituting (9), (10) and (11) into (2) yields the static equations of the continuum manipulator as follows:

$$K_k\theta_{i,k} = \begin{cases} \sum_{j=1}^{4} \boldsymbol{F}_{i,\text{front}}^{j} \times (\boldsymbol{P}_{i,k} - \boldsymbol{Q}_{i,j}) + \boldsymbol{F}^{\text{ext}} \times (\boldsymbol{P}_{i,k} - \boldsymbol{S}) i \le 7 \\ \boldsymbol{F}_{i,\text{front}}^{1} \times (\boldsymbol{P}_{i,k} - \boldsymbol{Q}_{i,4}) + \boldsymbol{F}_{i,\text{front}}^{4} \times (\boldsymbol{P}_{i,k} - \boldsymbol{Q}_{i,4}) + \boldsymbol{F}^{\text{ext}} \\ \quad \times (\boldsymbol{P}_{i,k} - \boldsymbol{S}) i > 7 \end{cases} \tag{12}$$

Here we contribute a simplified static equation, which do not have integration or differential terms and can be solved easily. The static model has been implemented in MATLAB using the "fsolve" function to solve the (12).

C. COMPUTATIONAL EFFICIENCY VERIFICATION

Compared with the traditional elliptic integral model [21], the computational efficiency of the static model based on the PRB 3R model is verified. Both static equations are solved by MATLAB's "fsolve" function. As shown in Table 1, the parameters of the PRB 3R model given in [25] are adopt. The CPU of the computer is Intel(R) Core(TM) i5-4590 CPU @ 3.30 GHz 3.30 GHz.

The driving force of the first cable changes from 10 N to 200 N in steps of 10 N, and the number of iterations is 20. As shown in Fig.7, the trajectory of the manipulator obtained by solving the two statics models is consistent. However, the solving efficiency of the PRB method is higher than the integral method. As shown in Table 2, the solving speed of the PRB method is 16.52 times faster than that of integral method, but the maximum error of the end trajectory obtained by the two methods is only 0.081%.

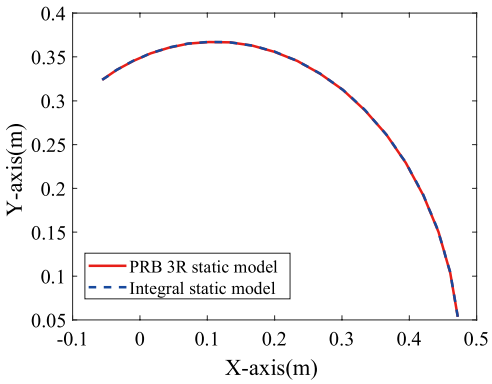

FIGURE 7. Comparison of the tip loci of the PRB 3R static model and the integral static model for continuum manipulator under a series of cable force.

III. ANALYSIS OF FRICTION AND STATIC COUPLING

There is a large amount of friction between drive cables and via holes, which has significant influence on the deformation movement of the continuum manipulator. On one hand, the friction between the cable and the via hole will cause the attenuation of the cable drive force, affecting the overall deformed shape of the compliant manipulator. On the other hand, the direction of the friction is also very important for the statically balanced configuration of the manipulator. The opposite direction of friction causes significant difference in configuration of the continuum manipulator. There is a static coupling between segments of the multi-segment compliant manipulator and the force of the rear segment is transmitted to the previous segment of the manipulator. Section-III-B analyzes the effects of manipulator configuration and stiffness on static coupling.

A. ANALYSIS OF FRICTION

1) EFFECT OF FRICTION ON BENDING CURVATURE

The constant curvature model assumes that the bending angles of all spring steel plates in each segment are the same.

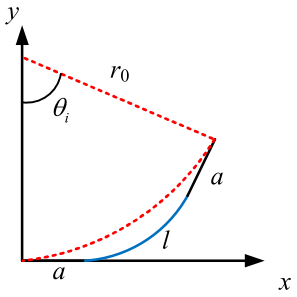

FIGURE 8. An illustration of the constant curvature model of one subsegment.

That is, when the bending angle of a segment is θ, the bending angle of each section is $\theta_i = \theta/\text{subseg}$. The constant curvature model of a subsegment is shown in Fig.8. To simplify the description, the spring steel plate and two devices for clamping spring steel plate are equivalent to the dotted arc in Fig.8. r_0 is the equivalent radius of the curvature.

As shown in Fig.8, the radius of curvature r_0 can be calculated by the geometric relations:

$$r_0 = \frac{l}{\theta_i} + \frac{a}{\tan\theta_i} + \frac{a}{\sin\theta_i}. \tag{13}$$

The homogeneous transformation matrix ${}^{i}\boldsymbol{T}$ of the ith subsegment from $\boldsymbol{O}_i$ to $\boldsymbol{O}_{i+1}$ can be obtained as follows:

$${}^{i}\boldsymbol{T} = \begin{bmatrix} \cos\theta_i & -\sin\theta_i & 0 & r_0\sin\theta_i + \text{distance}^*\cos\theta_i \\ \sin\theta_i & \cos\theta_i & 0 & r_0(1-\cos\theta_i) + \text{distance}^*\sin\theta_i \\ 0 & 0 & 1 & 0 \\ 0 & 0 & 0 & 1 \end{bmatrix}. \tag{14}$$

Using the static model, we can obtain the trajectory of the manipulator by changing the tension of the cable. Here, we change the tension of the 1th cable from 0 N to 150 N in steps of 1 N, and tensions of the other three cables are always zero. In Fig.9, the blue dotted line represents the trajectory of the end of the manipulator obtained by using the static model without friction, i.e., $\mu = 0$ in (6). The red dash-dotted line represents the trajectory of the end of the manipulator obtained by using static model with friction, and $\mu = 0.3$ in (6). The green solid line represents the trajectory of the end of the manipulator obtained by using the constant curvature model.

In Fig.9, we can find that the trajectory obtained by the frictionless static model is consistent with the constant curvature model. This conclusion coincides with the conclusion drawn from [23]. This is because, without the friction, the tension of the cable would be uniformly distributed over the entire manipulator. The solutions of the static equation of each subsegment are exactly the same. Fig.10 shows the position error of the end trajectory obtained by the static model considering the friction and the end trajectory obtained by the constant curvature model in the Y-axis direction. When theta is greater than 80 deg, the position error in Y direction is larger than 2%.

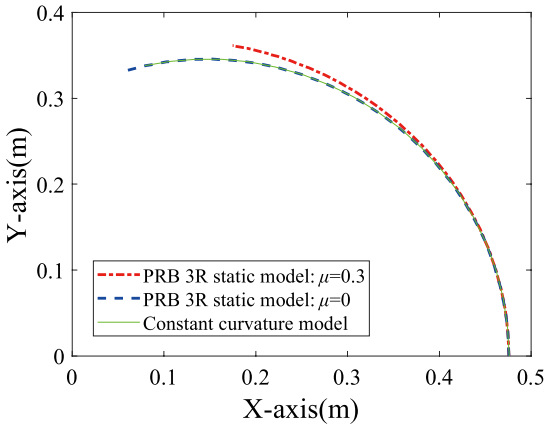

FIGURE 9. Comparison of the tip trajectory of the PRB 3R static model with friction and without friction and the constant curvature model for continuum manipulator.

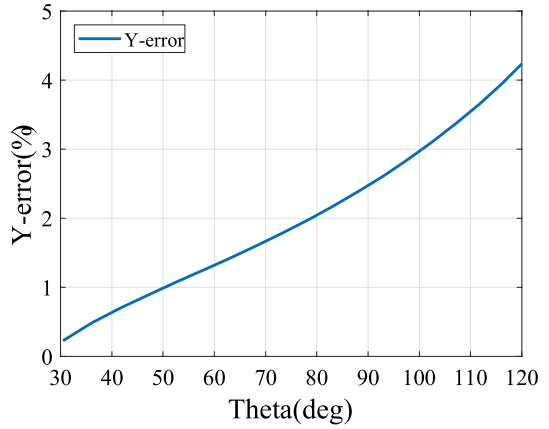

FIGURE 10. Error of disk positions in Y direction.

Therefore, if the friction force is large, using the constant curvature model to predict the motion will lead to a big error.

2) DIFFERENT DIRECTION OF FRICTION EFFECTS

As shown in (6), the value of s will affect the calculation of the transferring force. We give Cables 1 and 3 different pulling sequences to discuss the effect of the change of the direction of friction on the multi-segment manipulator. Similar to Experiment 2, the way of obtaining the experimental data will be introduced in Section IV.

Fig.11 illustrates the configuration of the manipulator of the tension of cables' applying order is different. The solid and dotted lines in the figure are the configuration of the manipulator in two different directions of friction. When the direction of the frictional force is reversed, the configuration of the manipulator changes dramatically. The displacement of the tip reaches 80.47 mm and the position error reaches 17.6%. It shows that the influence of friction force is significant in the multi-segment manipulator. The maximum absolute position error of 4.24% in this experiment is seen in Disk 14 for the 2.5 kg actuation case. Fig.12 shows the

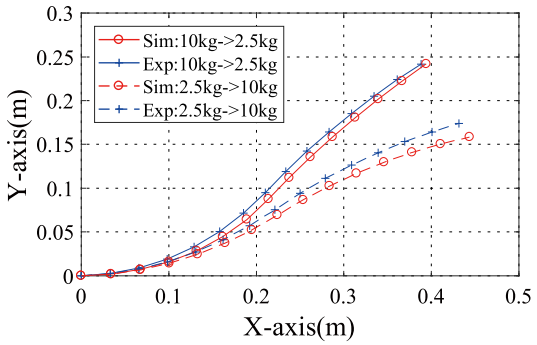

FIGURE 11. Displacement of Disk 7 between two configurations with different friction directions.

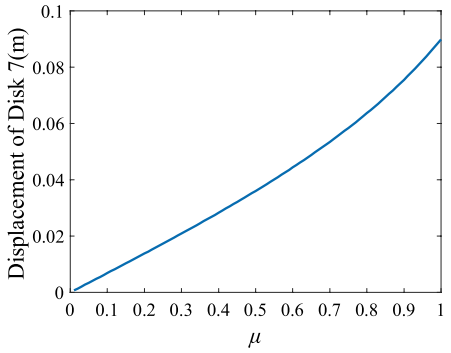

FIGURE 12. Comparison of simulation data and experimental data of PRB 3R static model with different friction directions.

effect of different friction coefficients when the sequence of the driving force is changed. We define this effect as the displacement of Disk 7 in these two sequences. The larger the displacement is, the greater the impact is. The relationship is approximately linear.

B. ANALYSIS OF STATIC COUPLING BETWEEN TWO SEGMENTS

In this section, we will discuss the coupling relationship of the multi-segment continuum manipulator. Since external loading affects both segments, it will not be considered in the discussion. On the other hand, if the stiffness of the Segments 1 and 2 is different, the coupling effect between the two segments will also be different. Taking these two aspects into account, (12) can be rewritten as follows:

$$K_{1,k}\theta_{i,k} = \sum_{j=1}^{4} \boldsymbol{F}^{j}_{i,\text{front}} \times (\boldsymbol{P}_{i,k} - \boldsymbol{Q}_{i,j}), \quad i \leq 7, \quad (15)$$

$$K_{2,k}\theta_{i,k} = \boldsymbol{F}^{1}_{i,\text{front}} \times (\boldsymbol{P}_{i,k} - \boldsymbol{Q}_{i,4}) + \boldsymbol{F}^{4}_{i,\text{front}} \times (\boldsymbol{P}_{i,k} - \boldsymbol{Q}_{i,4}), \quad i > 7, \quad (16)$$

where $K_{1,k}$ and $K_{2,k}$ are the stiffness coefficients of Segments 1 and 2, respectively.

Equations (15) and (16) show that the influence of Segment 2 on Segment 1 can be derived in many ways. As shown in (15), $\boldsymbol{F}^{1}_{i,\text{front}}$ and $\boldsymbol{F}^{4}_{i,\text{front}}$ should be considered when the static equation of Segment 1 is solved. First, if the initial configuration of Segment 1 is different, the difference will result in various directions of $\boldsymbol{PQ}$ and different initial force in the equation. Thus, the equation will attain multiple results. Second, different stiffness coefficients of Segments 1 and 2 will affect the result too. For example, when $K_{1,k}$ is large enough, $\boldsymbol{F}^{1}_{i,\text{front}}$ and $\boldsymbol{F}^{4}_{i,\text{front}}$ will have little inference on the solving of (15), since they are much smaller than $\boldsymbol{F}^{2}_{i,\text{front}}$ and $\boldsymbol{F}^{3}_{i,\text{front}}$, and it is enough to control Segment 2 to work.

1) EFFECT OF CONFIGURATION ON STATIC COUPLING

From (15) and (16), we know that the initial value of $\theta_{i,k}$ will affect the solution of the equation. By changing the initial value of $\theta_{i,k}(i \in [1\ 7])$, that is, the initial configuration of Segment 1, the influence of Segment 2 on Segment 1 under different initial configurations will be discussed. Meanwhile, the displacement of the end of Segment 1 between two states is defined as the magnitude of the impact.

By applying four different hanging weights 2.5 kg, 5 kg, 7.5 kg, and 10 kg on Cable 3, we control Segment 1 with four different initial configurations. Fig.13 shows the change of manipulator with four different initial configurations when we apply the constant force 10 N on Cable 1. The figure contains simulation data and experimental data. The way of obtaining the experimental data will be introduced in Section IV. From these four results, the initial configuration of Fig.13 (a, b and c) has the similar displacement of Disk 7 : 0.0734 mm, 0.0728 mm and 0.0604 mm. However, the influence of Fig.13 (d) is reduced, which is only 0.0381 mm.

To discuss the phenomenon deeply, the displacement of Disk 7 with different initial configurations is simulated. Fig.14 shows the influence of Segment 2 with different initial configurations on Segment 1 from the simulation, where two different conditions (with friction and without friction) are applied. The displacement of Disk 7 is obtained by changing the tension of Cable 2 by step while the tension of Cable 4 is constant at 50 N. The displacements of Disk 7 are similar when Cable 2 is between 0 and 60 N. After the tension of the cable exceeds 60 N, the displacement of Disk 7 begins to decrease sharply. It can be concluded from this result that within a certain initial configuration range, the tension influence of constant Cable 4 on the first segment is similar. When we consider the friction in red line shown in Fig.14, a sharp decrease at the bending point corresponds to a straight configuration of Segment 1.

We can calculate that the frictional force is zero at this point. Meanwhile, we define the inflection point as the "*changing point*" which means the configuration of Segment 1 is straight and the friction of Segment 1 is zero. When the tension of Segment 1 increases, the bending angle will increase too. According to (6), it can be concluded that the friction will also increase. Therefore, starting from the *changing point*, with the increase of the tension of Cable 2, the influence of the tension of Cable 4 on Segment 1 decreases gradually.

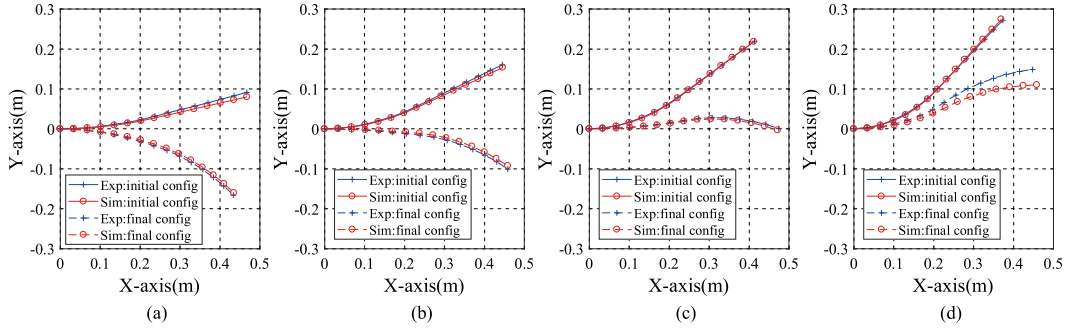

FIGURE 13. The effects of coupling under four different configurations.

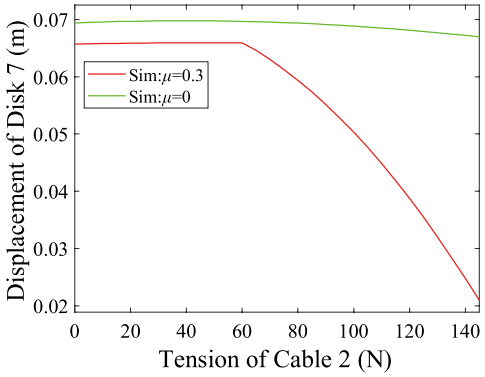

FIGURE 14. Displacement of Disk 7 of different tension of Cable 2 with and without friction.

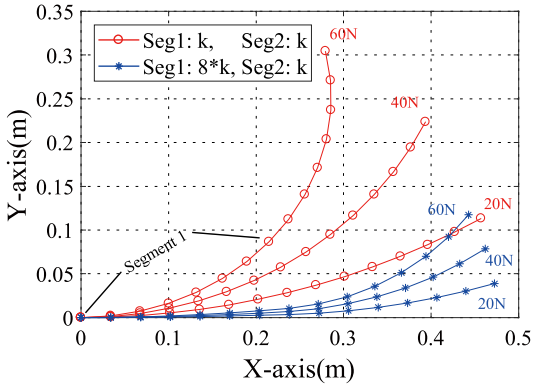

FIGURE 15. Comparison of different stiffness of Segment 1 for tensions of 20, 40, and 60 N in Cable 1.

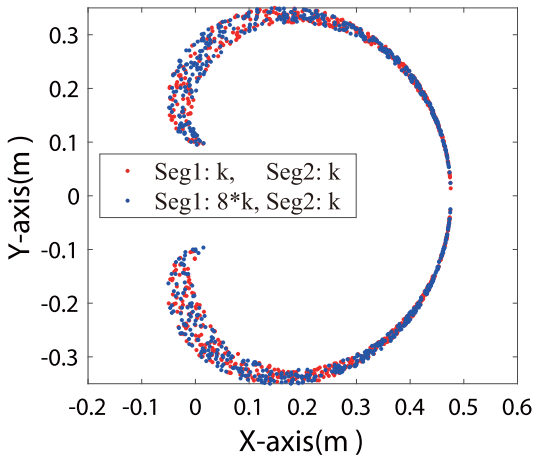

FIGURE 16. Comparison of the workspace of the continuum manipulator with different stiffness of Segment 1.

2) EFFECT OF STIFFNESS ON STATIC COUPLING

From (15) and (16), we know that the value of $K_{1,k}$ and $K_{2,k}$ affect the solution of the equation. We double the thickness h of these spring steels of Segment 1. Therefore, we can get a moment of inertia I of Segment 1 which is 2^3 =8 times that of the moment of inertia of Segment 2 according to the definition of I as follows:

$$I = \frac{bh^3}{12}, \tag{17}$$

where b is the width of the spring steel.

The driven cables' force of Segment 1 will be kept zero, and we increases the driving force of Cable 3 from 20 N to 40 N to 60 N, so as to obtain the configuration of the manipulator.

Fig.15 shows that the deformation is much smaller when $K_{1,k}$ is 8 times as large as $K_{2,k}$. The driving force of Segment 2 has much less effect on Segment 1 in this condition. Thus, when we design the multi-segment continuum manipulator, based on the results, the coupling effects between the two segments should be considered. Increasing the stiffness of Segment 1 can reduce the influence of Segment 2 on Segment 1.

The workspace analysis is carried out for these two manipulators, which are controlled by force, with different stiffness coefficients. To simplify the analysis, we only discuss the position of the tip in this section without the attitude.

Fig.16 shows part of the workspace of the two kinds of manipulator. It shows that the workspace of the continuum manipulator cannot be affected by the stiffness of the spring steel, but it needs a larger driving force to control the manipulator when the stiffness of the spring steel is increased.

Fig.17 shows the working space in case that the driving cables of Segment 1 is broken. The driving force applied to Segment 2 is the same as that in Fig.16. It can be seen that with the stiffness of 8 times k, the range of workspace

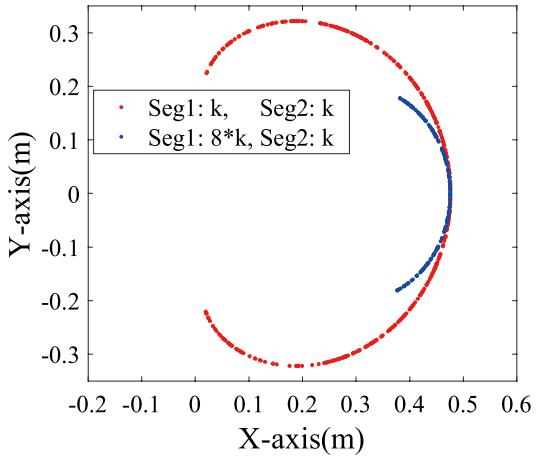

FIGURE 17. Comparison of the workspace of the continuum manipulator with different stiffness of Segment 1, when the driven cables of Segment 1 are broken.

is mainly decided by the movement of Segment 2. So the region of workspace is small. On the other hand, with the stiffness of k, the range of workspace is similar with that shown in Fig.16, which is much larger. The influence of different stiffness on the workspace of the manipulator shown in the two figures above shows that these two designs have different advantages and should be determined according to the actual needs.

IV. NUMERICAL SIMULATION AND EXPERIMENTAL RESULTS

In this section, experimental validation is used to verify the accuracy of the actuated case studies of the static model. Based on this model, the effects of friction and the relationship between multi-segment coupling are analyzed in detail.

A. EXPERIMENTAL SETUP

Fig.18 shows the experimental test platform utilized. The manipulator is assembled by 14 disks (6061 Aluminum Alloy, 0.056 m diameter, 0.004 m thickness) with a spring steel (ASTM 301EH, 0.030 m*0.030 m*0.0008 m in size) in each disk. The spring steel is fixed by screws between two disks. Cables (ASTM 304, 0.0012 m diameter) are tensioned using hanging weights routed over pulleys in the actuation module. External loads can be applied dynamically by hanging weights using a pulley and a guide rail parallel to the X-axis. We control the speed of the weights to be slow enough, which is less than 5 cm/s, to ensure that the manipulator would not vibrate and that the direction of the frictional force would keep the same. A CMOS camera (HT-UB1000, Shenzhen, China) is used to capture the images as required. Create a camera collection point at the top of each disk and place the calibration target on the desk. For all case studies, the material and geometric properties of the manipulator have been detailed in Table 3.

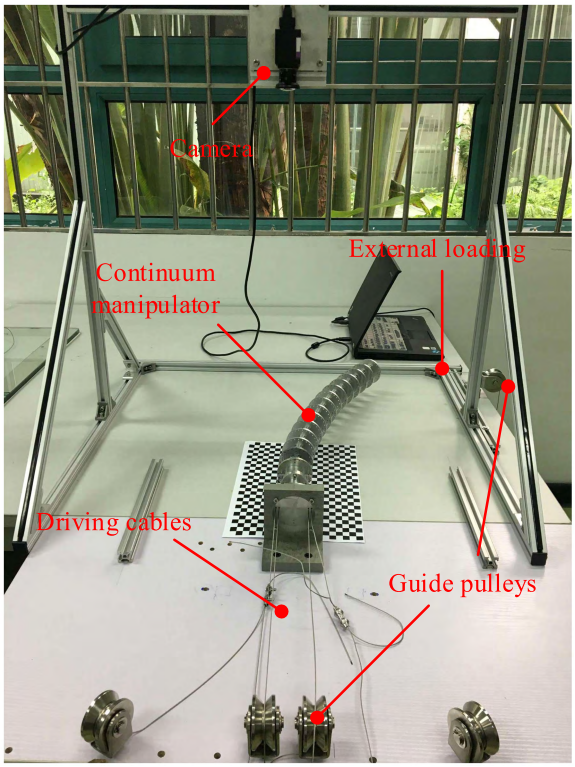

FIGURE 18. Prototype used for experimental validation. Cables are tensioned using hanging weights routed over pulleys in the actuation module.

TABLE 3. The comparation of the prb 3r model and the integral model in computation speed.

Symbol	Property	Value
E	Spring steel Young's Modulus	$1.71 \cdot 10^{11}$ Pa
I	Spring steel Moment of Inertia	$1.28 \cdot 10^{-12}$ kg·m^2
$d1$	Inside Routing Hole Radius	0.021 m
$d2$	Outside Routing Hole Radius	0.0255 m
g	Gravitational Acceleration	9.785 m/s^2
a	Clamping Structure Length	0.008 m
μ	Coefficient of Friction	0.3

B. EXPERIMENTAL RESULTS

1) EXPERIMENT 1: ONE ACTUATION VALIDATION

Fig.19 shows the experimental results for a range of actuation weights ranging from 2.5 kg to 10 kg in the single actuation case. We collect 10 experimental data of each weight. Fig.20 quantifies the percent error of the disk positions of the PRB 3R static equilibrium relative to the experimental results (a positive error correlates to "overshooting" the experimental configuration, like the 7.5 kg case). The error bar is used to show the fluctuation of the same experimental condition. Since the static friction coefficient of the manipulator in the stable state is variational and the tendon loading history of each experiment of the manipulator is not exactly the

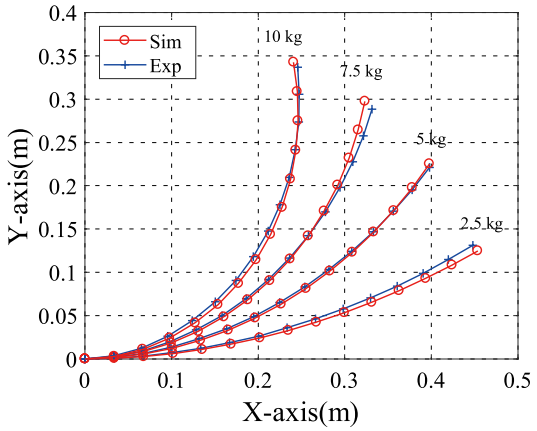

FIGURE 19. Comparison of the experimentally measured static equilibrium and the calculated PRB 3R static model equilibrium for weights of 2.5, 5, 7.5, and 10 kg in Cable 1.

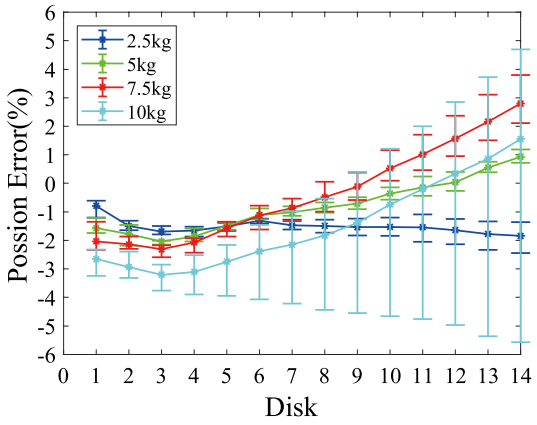

FIGURE 20. Error and error bar of disk positions relative to the experimentally measured disk positions for actuation weights of 2.5, 5, 7.5, and 10 kg in Cable 1.

TABLE 4. The tension of cables in three cases.

Cable number	Case 1	Case 2	Case 3
Cable 1	2.5 kg	5 kg	2.5 kg
Cable 3	10 kg	10 kg	5 kg

same [8], the error fluctuation of 10 kg case is large. The maximum absolute position error is found to be 5.57%.

2) EXPERIMENT 2: TWO SEGMENTS COUPLING VALIDATION

There are three cases of different weights suspended on Cable 1 which can actuate Segment 1 to the positive direction of Y axis and Cable 3 which can actuate Segment 2 to the negative direction of Y axis, as shown in Table 4.

Segment 1 is driven firstly, then Segment 2. During all the experiments, we can ensure that the directions of frictions are the same because of the low driving speed. Fig.21 illustrates the experimental results and the calculated static equilibria

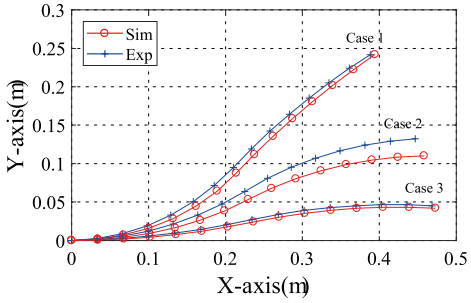

FIGURE 21. Comparison of the experimentally measured static equilibrium and the calculated PRB 3R static model equilibrium for Cases 1, 2, and 3.

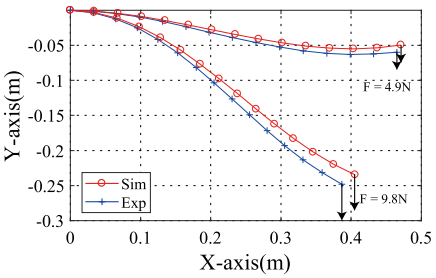

FIGURE 22. Comparison of the static equilibrium measured experimentally and the calculated PRB static model equilibrium for external loading 4.9 N and 9.8 N.

for the loading described in Table 4. The maximum absolute position error of 5.39% is seen in Disk 9 for Case 2.

3) EXPERIMENT 3: EXTERNAL LOADING VALIDATION

A constant weight of 5 kg is attached to Cable 1, and as shown in Fig.18 the tension along the negative direction of Y axis is applied to the tip of the manipulator. The external loading in two experiments are 0.5 kg and 1 kg, respectively.

Fig.22 illustrates the configuration of the manipulator with different external loadings. From the experimental results, the PRB 3R static model can well predict the shape of the manipulator under external loading, and also take into account the effect of friction. The maximum absolute position error of 5.04% is seen in Disk 14 for the 1 kg external loading case.

C. ERROR ANALYSIS

As shown in the previous experimental results, simulation calculation can predict the experimental results well. It has validated the proposed PRB 3R static model too. However, there are some obvious errors affecting the experiment. We summarize the sources of error as follows:

1) Assembly error of the manipulator. All of the center of disks may not be completely on the same horizontal surface, causing the cable tension not to be strictly horizontal;

2) The static friction force between the cable and the fixed pulley and the static friction force between the fixed pulley and the bearing will also influence the measurement of the experimental results. Even if the fixed pulley is lubricant enough and the coefficient of friction between them is small;

3) Assumption in Section II.B is not applicable to the actual situation well, since the friction force at the equilibrium state is static friction force instead of the dynamic friction force.

V. CONCLUSION

A new static analysis method for cable-driven continuum manipulator based on PRB 3R model is developed. This method transforms the continuum manipulator into the traditional rigid manipulator structure for analyzing and solving the problem of low computational efficiency caused by the integral term of the traditional beam theoretical mechanics model. The static equation of the multi-segment continuum manipulator based on PRB 3R method has high precision and can be solved efficiently. This method is also used to analyze the influence of friction force, multi-segment coupling and external loading on the continuum manipulator. Meanwhile, some related experiments are conducted to verify the accuracy of the modeling method. In the future, we will study dynamic model of three dimensional cable-driven continuum manipulator based on the PRB 3R model.

ACKNOWLEDGMENT

(Shaoping Huang and DESHAN MENG contributed equally to this work.)

REFERENCES

[1] S. Aziz, "Lessons learned from the STS-120/ISS 10A robotics operations," *Acta Astronaut*, vol. 66, nos. 1–2, pp. 157–165, Feb. 2010.
[2] F. Feng, L. Tang, J. Xu, H. Liu, and Y. Liu, "A review of the end-effector of large space manipulator with capabilities of misalignment tolerance and soft capture," *Sci. China Technol. Sci.*, vol. 59, no. 11, pp. 1621–1638, 2016.
[3] P. Laryssa *et al.*, "International space station robotics: A comparative study of ERA, JEMRMS and MSS," in *Proc. 7th ESA Workshop Adv. Space Technol. Robot. Autom.*, Noordwijk, The Netherlands, Nov. 2002, pp. 1–8.
[4] G. Robinson and J. B. C. Davies, "Continuum robots—A state of the art," in *Proc. IEEE Int. Conf. Robot. Automat. (ICRA)*, Detroit, MI, USA, May 1999, pp. 2849–2854.
[5] I. D. Walker, "Continuous backbone 'continuum' robot manipulators," *ISRN Robot.*, vol. 2013, May 2013, Art. no. 726506.
[6] R. J. Webster, III, and B. A. Jones, "Design and kinematic modeling of constant curvature continuum robots: A review," *Int. J. Robot. Res.*, vol. 29, no. 13, pp. 1661–1683, 2010.
[7] T. Mahl, A. E. Mayer, A. Hildebrandt, and O. Sawodny, "A variable curvature modeling approach for kinematic control of continuum manipulators," in *Proc. Amer. Control Conf. (ACC)*, Washington, DC, USA, Jun. 2013, pp. 4945–4950.
[8] A. Gao, Y. Zou, Z. Wang, and H. Liu, "A general friction model of discrete interactions for tendon actuated dexterous manipulators," *J. Mechan. Robot.*, vol. 9, no. 4, p. 041019, 2017.
[9] D. C. Rucker and R. J. Webster, III, "Statics and dynamics of continuum robots with general tendon routing and external loading," *IEEE Trans. Robot.*, vol. 27, no. 6, pp. 1033–1044, Dec. 2011.
[10] R. J. Webster, III, J. M. Romano, and N. J. Cowan, "Mechanics of precurved-tube continuum robots," *IEEE Trans. Robot.*, vol. 25, no. 1, pp. 67–78, Feb. 2009.
[11] D. C. Rucker, *The Mechanics of Continuum Robots: Model-Based Sensing and Control*. Nashville, TN, USA: Vanderbilt Univ., 2011, pp. 94–107.
[12] D. C. Rucker, R. J. Webster, III, G. S. Chirikjian, and N. J. Cowan, "Equilibrium conformations of concentric-tube continuum robots," *Int. J. Robot. Res.*, vol. 29, no. 10, pp. 1263–1280, 2010.
[13] L. L. Howell, *Compliant Mechanisms*. New York, NY, USA: Wiley, 2001, pp. 42–55.
[14] W. S. Rone and P. Ben-Tzvi, "Continuum robot dynamics utilizing the principle of virtual power," *IEEE Trans. Robot.*, vol. 30, no. 1, pp. 275–287, Feb. 2014.
[15] D. C. Rucker, B. A. Jones, and R. J. Webster, III, "A geometrically exact model for externally loaded concentric-tube continuum robots," *IEEE Trans. Robot.*, vol. 26, no. 5, pp. 769–780, Oct. 2010.
[16] H. Yuan and Z. Li, "Workspace analysis of cable-driven continuum manipulators based on static model," *Robot. Comput.-Integr. Manuf.*, vol. 49, pp. 240–252, Feb. 2018.
[17] H. Yuan, P. W. Y. Chiu, and Z. Li, "Shape-reconstruction-based force sensing method for continuum surgical robots with large deformation," *IEEE Robot. Autom. Lett.*, vol. 2, no. 4, pp. 1972–1979, Oct. 2017.
[18] W. S. Rone and P. Ben-Tzvi, "Mechanics modeling of multisegment rod-driven continuum robots," *J. Mechan. Robot.*, vol. 6, no. 4, p. 041006, 2014.
[19] J. Jung, R. S. Penning, N. J. Ferrier, and M. R. Zinn, "A modeling approach for continuum robotic manipulators: Effects of nonlinear internal device friction," in *Proc. IEEE/RSJ Int. Conf. Intell. Robots Syst. (IROS)*, San Francisco, CA, USA, Sep. 2011, pp. 5139–5146.
[20] G. Subramani and M. R. Zinn, "Tackling friction—An analytical modeling approach to understanding friction in single tendon driven continuum manipulators," in *Proc. IEEE Int. Conf. Robot. Autom. (ICRA)*, Seattle, WA, USA, May 2015, pp. 610–617.
[21] H.-J. Su, "A pseudorigid-body 3R model for determining large deflection of cantilever beams subject to tip loads," *J. Mechan. Robot.*, vol. 1, no. 2, p. 021008, 2009.
[22] A. Saxena and S. N. Kramer, "A simple and accurate method for determining large deflections in compliant mechanisms subjected to end forces and moments," *ASME J. Mech. Des.*, vol. 120, no. 3, pp. 392–400, 1998.
[23] I. A. Gravagne, C. D. Rahn, and I. D. Walker, "Large deflection dynamics and control for planar continuum robots," *IEEE/ASME Trans. Mechatronics*, vol. 8, no. 2, pp. 299–307, Jun. 2003.
[24] T. R. de Oliveira and N. A. Lemos, "Force and torque of a string on a pulley," *Amer. J. Phys.*, vol. 86, no. 4, pp. 275–279, Apr. 2018.
[25] G. Chen, B. Xiong, and X. Huang, "Finding the optimal characteristic parameters for 3R pseudo-rigid-body model using an improved particle swarm optimizer," *Precis. Eng.*, vol. 35, no. 3, pp. 505–511, 2011.

SHAOPING HUANG received the B.S. degree in applied physics from the Huazhong University of Science and Technology, Wuhan, China, in 2013. He is currently pursuing the M.S. degree in control engineering with the Graduate School at Shenzhen, Tsinghua University, China.

His research interest includes Robotics and dynamics and statics of continuum robot.

DESHAN MENG received the B.E. degree in mechatronics engineering from the Liaoning University of Science and Technology, Anshan, China, in 2011, and the master's and Ph.D. degrees in control science and engineering from the Shenzhen Graduate School, Harbin Institute of Technology, Shenzhen, China, in 2013 and 2017, respectively.

He is currently a Post-Doctoral Researcher with the Shenzhen Graduate School, Tsinghua University, Shenzhen, China. His research interests include space robotics, continuum robotics, dynamic modeling, and control.

YU SHE received the bachelor's degree in mechanical engineering from the Taiyuan University of Technology, Taiyuan, China, in 2011, the master's degree in mechanical and automation from the Harbin Institute of Technology, Shenzhen, China, in 2014, and the Ph.D. degree in mechanical engineering from The Ohio State University, in 2018.

He currently works as a Post-Doctoral Associate with the Computer Science & Artificial Intelligence Laboratory, Massachusetts Institute of Technology. His research interests include design, compliant mechanisms, mechatronics, mobile robots, soft robots, and Physical Human–Robot Interaction.

XUEQIAN WANG received the B.E. degree from the mechanical design manufacturing and automation, Harbin University of Science and Technology, Harbin, China, in 2003, the M.E. degree from the Department of Mechatronics and Automation in 2006, and the Ph.D. degrees in control science and engineering from the Shenzhen Graduate School, Harbin Institute of Technology, Shenzhen, China, in 2010.

He is currently an Associate Professor with the Shenzhen Graduate School, Tsinghua University, Shenzhen. His research interests include space robotics and teleoperation.

BIN LIANG (M'97) received the B.S. and the M.S. degrees in control engineering from Northwestern Polytechnical University, Xi'an, China, in 1991 and 1994, respectively, and the Ph.D. degree in precision instrument and mechanology from Tsinghua University, Beijing, China, in 1994.

He is currently a Professor with the Department of Automation, Tsinghua University, Beijing. His research interests include space robotics, manipulators, and intelligent control.

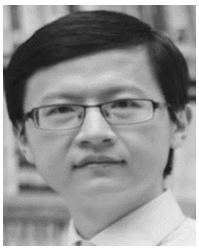

BO YUAN (S'02–M'07) received the B.E. degree in computer science from the Nanjing University of Science and Technology, China, in 1998, and the M.Sc. and Ph.D. degrees in computer science from The University of Queensland, Australia, in 2002 and 2006, respectively.

From 2006 to 2007, he was a Research Officer with The University of Queensland. Since 2007, he has been with the Graduate School at Shenzhen, Tsinghua University, China, where he is currently an Associate Professor. He has authored over 80 research articles, and is the inventor of four patents. His research interests include data analytics, evolutionary computation, and GPU computing.